

# Anion-Derived Solid Electrolyte Interphase Enabled by Diluent Modulated Dimethyl Carbonate-Based Localized High Concentration Electrolytes for Lithium Metal Batteries

Hanlu Zheng,<sup>[a]</sup> Yu Zhong,<sup>[a]</sup> Changdong Gu,<sup>[a]</sup> Xiuli Wang,<sup>\*[a]</sup> and Jiangping Tu<sup>\*[a]</sup>

Carbonate-based electrolytes generally suffer from low Coulombic efficiency and poor cycling stability in lithium metal batteries. In this work, localized high concentration electrolytes (LHCEs) based on dimethyl carbonate (DMC) with varying diluent additions are designed. LHCEs demonstrate higher Li<sup>+</sup> transference numbers and a greater proportion of contact ion pairs (CIPs) and ion pair aggregates (AGGs) in the solvation structures, facilitating the formation of anion-derived solid

electrolyte interphase (SEI). Furthermore, LHCEs enhance the Coulombic efficiency of Li||Cu cells and improve the anodic stability against lithium. One of these LHCEs, prepared with appropriate diluent addition, exhibits excellent capacity retention in Li||NCM622 cells at 0.5 C after 150 cycles, thus presenting promising possibilities for the development of high energy density lithium metal batteries.

## Introduction

Lithium ion batteries (LIBs) have been widely applied to various fields, such as portable electronics, electric vehicles and grid-energy storage systems. Most of the electrolytes currently used in commercial LIBs are liquid electrolytes, which have better wetting of electrode surface and higher ionic conductivity. However, current commercial batteries are no longer able to meet the growing demand for electronics and vehicles, so there is an urgent need to develop batteries with higher safety, higher energy density, longer cycle life, and lower cost. Lithium metal, with its ultra-high capacity (3860 mAh g<sup>-1</sup>), low density (0.59 g cm<sup>-3</sup>), and lowest electrode potential (-3.040 V vs. standard hydrogen electrode), is valuable for preparing LIBs with higher energy density.<sup>[1]</sup> However, unstable SEI and uncontrolled dendrite growth have hindered the practical application of lithium metal anodes.<sup>[2]</sup>

High concentration electrolyte (HCE) is a promising method for stabilizing lithium metal anodes recently.<sup>[3-5]</sup> Distinguished from conventional LCE, which are dominated by free solvent molecules, the increase in salt concentration reduces the amount of free solvent in the electrolyte, and enhances the interactions between cations and anions, and almost all solvent molecules and anions are coordinated to lithium ions, contributing to the formation of inorganic-rich SEI.<sup>[6-7]</sup> Owing to the special solvation structure, HCE has a wide electrochemical window,<sup>[8-9]</sup> low flammability,<sup>[10-11]</sup> and an anion-derived SEI inhibits the lithium dendrite formation and growth,<sup>[11]</sup> providing

advantages for the development of high-performance lithium batteries. However, HCE suffers from high viscosity and cost, which hinder its commercialization. Introducing an inert diluent to prepare LHCEs is expected to overcome these shortcomings of HCEs.<sup>[12-14]</sup> This diluent can be miscible with the solvent, but does not coordinate with the lithium ions,<sup>[15]</sup> allowing it to maintain the special solvation structure of HCE in a localized environment and inherit its excellent electrochemical performance,<sup>[16-17]</sup> such as a wide electrochemical window; simultaneously, the use of the inert diluent also reduces the lithium salt content in the electrolyte, effectively mitigating the drawbacks of HCE in terms of viscosity, wettability, and cost.<sup>[15-16]</sup> Hence, LHCE holds promising prospects for various applications. 1,1,2,2-tetrafluoroethyl-2,2,3,3-tetrafluoropropyl ether (TTE), as a commonly used diluent, has been widely employed. The fluorinated chain of TTE offers weak solvation ability due to significant steric hindrance and electron-withdrawing groups (-CF<sub>2</sub>-). Watanabe's group utilized TTE as a diluent to design a LHCE (LiTFSI-G<sub>4</sub>-4TTE, by mol.), aiming to mitigate the "shuttle effect" of polysulfides in lithium-sulfur batteries, resulting in higher Coulombic efficiency and cycling stability.<sup>[18]</sup> Ren et al. designed a sulfone-based LHCE (LiFSI-3TMS-3TTE, by mol.), which significantly suppressed the decomposition of the electrolyte on the lithium metal anode, and addressed the issue of corrosion on aluminum foil surfaces caused by high concentration electrolytes (HCE) under high voltage, enabling stable cycling of 3.2–4.9 V Li||LNMO batteries for over 100 cycles.<sup>[19]</sup>

Moreover, conventional carbonate electrolytes are incompatible with alkali metal anodes,<sup>[20]</sup> and display poor anodic stability at high voltages, resulting in significant electrolyte decomposition.<sup>[21]</sup> In particular, the electrolytes containing fluorinated solvents can overcome many issues associated with traditional electrolytes, including interfacial instability, rapid capacity degradation at extreme temperatures, and high flammability.<sup>[22]</sup> Fluorinated ethylene carbonate (FEC) serves as

[a] H. Zheng, Y. Zhong, C. Gu, X. Wang, Prof. J. Tu

State Key Laboratory of Silicon and Advanced Semiconductor Materials, School of Materials Science and Engineering, Zhejiang University, Hangzhou 310027, China

E-mail: wangxl@zju.edu.cn

tujp@zju.edu.cn

 Supporting information for this article is available on the WWW under <https://doi.org/10.1002/batt.202400238>

a commonly used additive to form LiF-rich SEI with low interfacial impedance.<sup>[23]</sup> Due to its low lowest occupied molecular orbital (LUMO), FEC decomposes preferentially, inevitably leading to form a LiF-rich or F-containing interface, providing high chemical and mechanical stability. However, the effectiveness of FEC as an additive often diminishes rapidly due to its quick consumption.

In this present work, we choose dimethyl carbonate (DMC) as the solvent, FEC as an additive, and TTE as a diluent to prepare LHCEs with different diluent ratios. The LHCEs broaden the electrochemical window and enhance the ion transference number by binding the anions through a unique solvation structure. It is found that excessive diluent leads to a stronger coordination between  $\text{Li}^+$  and the solvent, which increases the organic component of SEI formed by solvent decomposition and reduces the F content within the SEI, thus affecting the anodic stability against Li and long-term cycling performance of the lithium metal batteries (LMBs). Therefore, the diluent addition is also a parameter worthy of significant attention in designing LHCEs. By selecting the appropriate diluent addition, we have designed an LHCE that improves the Coulombic efficiency of carbonate-based electrolytes and the cycling stability against lithium metal anode. Furthermore, it exhibits excellent capacity retention in  $\text{Li} \parallel \text{NCM}622$  cells at 0.5 C after 150 cycles.

## Experimental Section

Table 1 summarizes the formulae used in the experiment. Lithium bis(fluorosulfonyl) imide (LiFSI) is dissolved in DMC solvent with FEC additive to yield the HCE (5 mol L<sup>-1</sup> LiFSI in DMC:FEC = 9:1), and then TTE diluent is added into the HCE in varying ratios to obtain the LHCE (coded as LHCE-2:1, LHCE-1:1 and LHCE-1:2, representing the ratios of the total solvent and additive amount to the diluent). Additionally, we prepare low concentration electrolyte (LCE, 1 mol L<sup>-1</sup> LiFSI in DMC:FEC = 9:1) with the same proportions of the solvent and the additive for comparison. Table 1 shows the specific molar ratios of solvent, additive, and diluent used in the experiment.

Table 2 summarizes the highest occupied molecular orbital (HOMO), lowest unoccupied molecular orbital (LUMO), dielectric constant ( $\epsilon$ ), donor number (DN), melting point (MP), boiling point (BP), and viscosity ( $\eta$ ) of the solvents used in the LHCEs. In general, solvents with lower LUMO are preferentially reduced and decomposed to form SEI.<sup>[24]</sup> From Table 2, it can be seen that HOMO and LUMO of FEC are lower than those of EC and DMC, indicating that FEC exhibits higher oxidative stability and is more easily reduced at the anode.

**Table 1.** Electrolyte formulae are used in the experiment.

Code	Electrolyte formulae
LHCE-2:1	2.67 mol L <sup>-1</sup> LiFSI in DMC:FEC:TTE = 9:1:5 by mol.
LHCE-1:1	1.81 mol L <sup>-1</sup> LiFSI in DMC:FEC:TTE = 9:1:10 by mol.
LHCE-1:2	1.10 mol L <sup>-1</sup> LiFSI in DMC:FEC:TTE = 9:1:20 by mol.
HCE	5.00 mol L <sup>-1</sup> LiFSI in DMC:FEC = 9:1 by mol.
LCE	1.00 mol L <sup>-1</sup> LiFSI in DMC:FEC = 9:1 by mol.

First, cathode materials LiFePO<sub>4</sub> (LFP), Super P, and polyvinylidene fluoride (PVDF) were ground and mixed at a mass ratio of 8 : 1 : 1, and then the solvent N-methylpyrrolidone (NMP) was added to the mixture. The resulting slurry was uniformly coated on the Al foil and dried at 80 °C for 24 h to obtain cathode for LMBs. CR2025-type coin cells were assembled in an argon (Ar) glove box ( $\text{O}_2 < 0.01$  ppm,  $\text{H}_2\text{O} < 0.01$  ppm). The mass loading of the LFP cathode is about 1.3 mg cm<sup>-2</sup>. Celgard 2500 was employed as the separator, and the amount of electrolyte for all tests was 50  $\mu\text{L}$ .

Raman spectra of electrolytes were recorded using a Thermo Scientific DXR with a 633 nm laser as the excitation light. The SEI and cathode electrolyte interphase (CEI) components were analyzed by Thermo Scientific K-Alpha X-ray photoelectron spectroscopy (XPS). The morphology observation of SEI was conducted by scanning electron microscopy (SEM), and before SEM analysis, the samples were washed with DMC solvent and dried at room temperature in an Ar-filled glove box. The  $\text{Li}^+$  transference numbers ( $t_{\text{Li}^+}$ ) of different electrolytes were determined using an electrochemical station with a potentiostatic polarization technique, in which a 10 mV overpotential was applied for 2000 s to a  $\text{Li} \parallel \text{Li}$  symmetrical cell. Electrochemical impedance spectroscopy (EIS) measurements of  $\text{Li} \parallel \text{Li}$  symmetrical cells were carried out in the frequency range 10<sup>5</sup> to 0.1 Hz. Linear sweep voltammetry (LSV) was conducted using an electrochemical station at a scan rate of 0.1 mV s<sup>-1</sup>.

## Results and Discussion

Ionic conductivity is one of the most important parameters for an electrolyte and is a key factor in determining the resistance and rate performance of a cell. Ionic conductivity is directly related to the salt concentration and electrolyte viscosity (Eq. 1).

$$\sigma = \sum \frac{(Z_i)^2 FC_i}{6\pi\eta r_i} \quad (1)$$

**Table 2.** Relevant physicochemical properties of the solvent in LHCE electrolytes.<sup>[25]</sup>

Solvent	HOMO/LUMO (eV)	$\epsilon$	DN (kcal mol <sup>-1</sup> )	MP/BP (°C)	P (g cm <sup>-3</sup> )	$\eta$ (mPa·s)
DMC	-8.18/-0.08	3.12	~17	4.6/91	1.07	0.59@25 °C
EC	-8.46/-0.26	89.78	~16	36.4/248	1.32	1.40@25 °C
FEC	-8.90/-0.37	89.6	9.1	18/249	1.454	-
TTE	-9.83/-0.36	2	< 10	-/92	1.533	-

where  $Z_i$  represents the charge number in the charging process,  $C_i$  is the molar concentration of salt, and  $F$  and  $\eta$  denote Faraday's constant and viscosity, respectively.  $r_i$  is the radius of the solvation ions.

The ionic conductivity of the four electrolytes is measured using an ionic conductivity meter (Figure 1e), revealing a correlation between the ionic conductivity and the addition ratio of the diluent. As the diluent content increases, the ionic conductivity decreases. LHCEs exhibit lower ion conductivity compared to LCE due to the viscosity. The phenomenon can be explained by Eq. 1, which shows that lower viscosity results in higher ionic conductivity, thus facilitating ionic diffusion. In fact, as the salt concentration increases, both the ionic conductivity and the ion self-diffusion coefficient of the solution decrease, not only due to an increase in viscosity, but also due to a change in the effective radius or transport mechanism of the lithium ions.<sup>[26]</sup> It is worth mentioning that the introduction of TTE also reduces the ionic conductivity, probably due to the fact that the non-solvating TTE outer shell creates a non-conducting medium in the electrolyte.<sup>[27]</sup> Thus, the high salt concentration and the addition of TTE diluent result in the ionic conductivity of LHCE less than that of LCE.

The  $\text{Li}^+$  transference number ( $t_{\text{Li}^+}$ ) is another significant parameter for the electrolytes. The increase in the  $\text{Li}^+$  transference number attenuates the concentration polarization during charging and discharging, thereby increasing the power density of the battery. As for commercial electrolytes, the conductivity is generally able to reach  $1\text{-}10 \text{ mS cm}^{-1}$ , but  $\text{Li}^+$  dissolved in the electrolyte undergoes solvation, and the solvation sheath restricts the migration rate of  $\text{Li}^+$ , while the anion hardly undergoes solvation, so the  $\text{Li}^+$  transference number of conventional electrolytes is generally lower than 0.5. In other words, the majority of the ionic conductivity is contributed by anions.<sup>[28]</sup> The low  $t_{\text{Li}^+}$  causes excessive anions

to accumulate on the surface of the cathode, creating a concentration gradient between the anode and the cathode. This gradient induces a concentration polarization in LIBs, leading to a large overpotential and limiting the improvement of the energy and power density of the LIBs.<sup>[29]</sup> In Figure 1, it can be seen that  $t_{\text{Li}^+}$  of LHCE is significantly higher than that of LCE, which may be attributed to the fact that the unique solvation structures of LHCEs make the mobility of anions considerably slower, while the effect on cations is small.

$$t_{\text{Li}^+} = \frac{I_s(\Delta V - I_0 R_0)}{I_0(\Delta V - I_s R_s)} \quad (2)$$

where  $I_0$  and  $I_s$  represent the initial and steady-state current values of the DC polarization test, respectively, while  $R_0$  and  $R_s$  denote the interface impedance values before and after DC polarization, respectively. Additionally,  $\Delta V$  refers to the DC polarization voltage, which in our work is set at 10 mV.

The  $t_{\text{Li}^+}$  of the electrolytes are calculated by assembling a  $\text{Li}||\text{Li}$  symmetric cell using the DC polarization method. It can be seen that LHCEs, despite sacrificing some of the ionic conductivity, notably elevate the  $\text{Li}^+$  transference number to above 0.5, while  $t_{\text{Li}^+}$  of LCE is below 0.5. The higher  $t_{\text{Li}^+}$  signifies a greater proportion of  $\text{Li}^+$  among the migrating ions in the electrolyte, which helps to weaken the reverse electric field generated by the anions within the electrolyte, and contributes to the reduction of the polarization of the cells.<sup>[30]</sup>

The LSV curves in Figure 1f show that LHCE-2:1 and LHCE-1:1 have a wide electrochemical window, which indicates that the LHCEs inherit the advantage of the HCE to broaden the electrochemical window. The primary factor is the significant reduction of free solvent molecules in LHCEs, thereby diminishing the occurrence of solvent-cation reactions. However, for LHCE-1:2, an oxidative decomposition peak appears at 4.3 V,

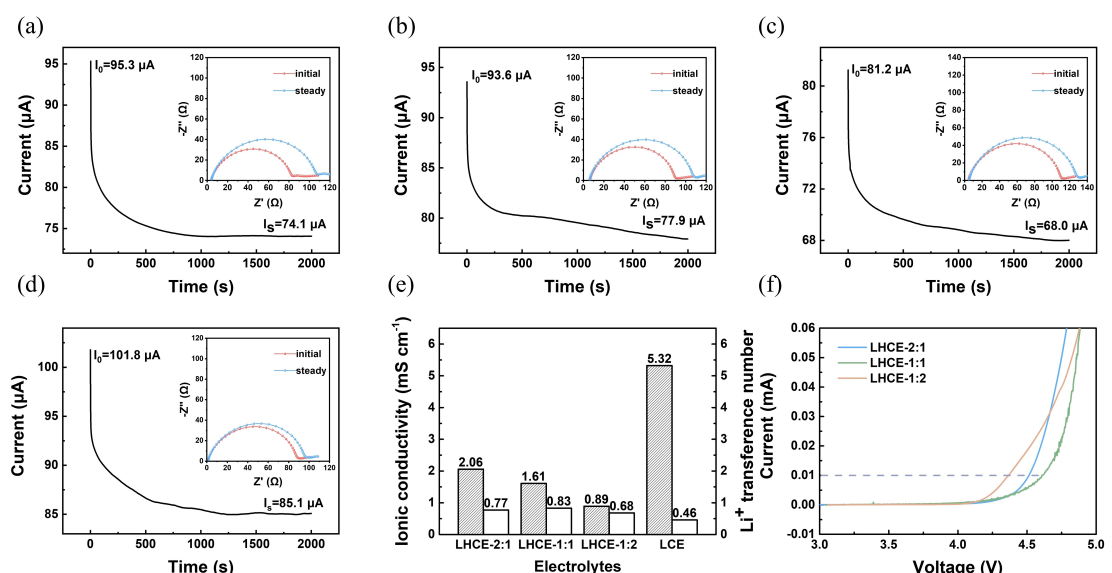


**Figure 1.** Current-time curve of  $\text{Li}||\text{Li}$  cell at a DC polarization of 0.01 V, inset: Nyquist plots of the cell before and after polarization, (a) LHCE-2:1; (b) LHCE-1:1; (c) LHCE-1:2; (d) LCE. (e) Ionic conductivity of four electrolytes and  $\text{Li}^+$  transference number calculated according to Eq. 2; (f) LSV curves of  $\text{Li}||\text{SS}$  cells using different electrolytes.

indicating that excessive diluent adversely affects the electrochemical stability of the electrolyte.

The Raman spectra in Figure 2a reveal that in the LHCEs, the solvent peaks of free solvent DMC and FEC exhibit a blue shift compared to LCE, indicating a transition of solvent from free-state to coordinated-state. The reduction in free solvent is beneficial for alleviating solvent decomposition during battery charge and discharge processes, thereby reducing the formation of organic-rich SEI caused by solvent decomposition. Moreover, coordinated FEC (Coord. FEC) and coordinated DMC (Coord. DMC) show continued blue shifts in the solvent peaks with the diluent ratios increasing, suggesting that with the increase in diluent, the dipole-dipole interactions between the solvent and diluent are enhanced, leading to stronger interactions experienced by the solvent. There are three common solvation configurations, including solvent-separated ion pairs (SSIPs), contact ion pairs (CIPs), and cation-anion aggregates (AGGs). In traditional commercial electrolytes, SSIP dominates in the solvation structure, so that many free solvent molecules and anions can be observed. The SSIP solvation structure leads to two problems: one is that the solvent decomposition does not allow to form a stable interface, which is the reason why we introduce FEC here to assist the generation of SEI and CEI;<sup>[31]</sup> and the other is that the presence of free solvent molecules leads to low oxidative stability.<sup>[32]</sup> As the salt concentration increases, the anions appear in the primary solvation sheath of the cations, forming a CIP or AGG structure, which accelerates formation of the LiF-rich interfacial layer, thereby stabilizing both cathode and anode. Li et al. revealed a unique micelle-like structure in LHCE, defining the more coordinated ion-pair aggregates as AGG+.<sup>[33]</sup> The solvation structures of three LHCEs and the LCE are tested by Raman spectroscopy (Figure 2b, 2c).

As shown in Figure 2b, SSIP and CIP dominate in LCE, whereas AGG and AGG+ dominate in LHCE. The proportion of AGG+ in LHCE-1:2 is higher than that in LHCE-2:1, indicating that the  $\text{Li}^+$ - $\text{FSI}^-$  binding was stronger. The solvation layer of Li ions of LHCE contains a large number of AGGs (Figure 2c), and this solvation configuration leads to the preferential reduction of anions to form LiF-rich SEI, which have good stability during Li plating/stripping and help to achieve homogeneous Li deposition and prevent the growth of Li dendrites. The schematic diagrams of the three solvation structures are shown in Figure 2d. SSIP reveals that Li ions are scarcely coordinated with anions; instead, they are typically surrounded by solvent molecules. In CIP, one  $\text{Li}^+$  is coordinated with one  $\text{FSI}^-$ , while in AGG, two or more  $\text{Li}^+$  are coordinated with one  $\text{FSI}^-$ .

To further investigate the effect of diluent on LHCEs, radial distribution functions (RDFs)  $g(r)$  and coordination number  $N(r)$  are obtained by molecular dynamics (MD). Here, LHCEs are compared with HCE rather than LCE to explore the impact of the diluent on solvation structures and coordination numbers. The snapshots of spatial distribution of HCE and LHCEs from MD simulations are shown in Figure 3a–d. The results demonstrate that  $\text{Li}^+$ ,  $\text{FSI}^-$  and solvent tend to aggregate to form clusters while diluent seldom coordinate with  $\text{Li}^+$  or  $\text{FSI}^-$ . In the RDF (Figure 3e–h), the peaks of  $\text{Li}-\text{O}_{\text{FSI}}$  all lie at 1.93 Å, with coordination numbers of 1.17, 1.31, 1.29 and 1.32 Å, respectively. In LHCEs, the coordination numbers of  $\text{Li}-\text{O}_{\text{FSI}}$  are all higher than HCE, aligning with the solvation structure of LHCEs dominated by CIPs and AGGs as demonstrated by the Raman spectra. Furthermore, the peak of  $\text{Li}-\text{O}_{\text{FSI}}$  is slightly closer  $\text{Li}-\text{O}_{\text{DMC}}$ , and the coordination number is higher, indicating a strong coordination between  $\text{Li}^+$  and  $\text{FSI}^-$ , which contributes to the formation of an anion-derived SEI. Additionally, in HCE and

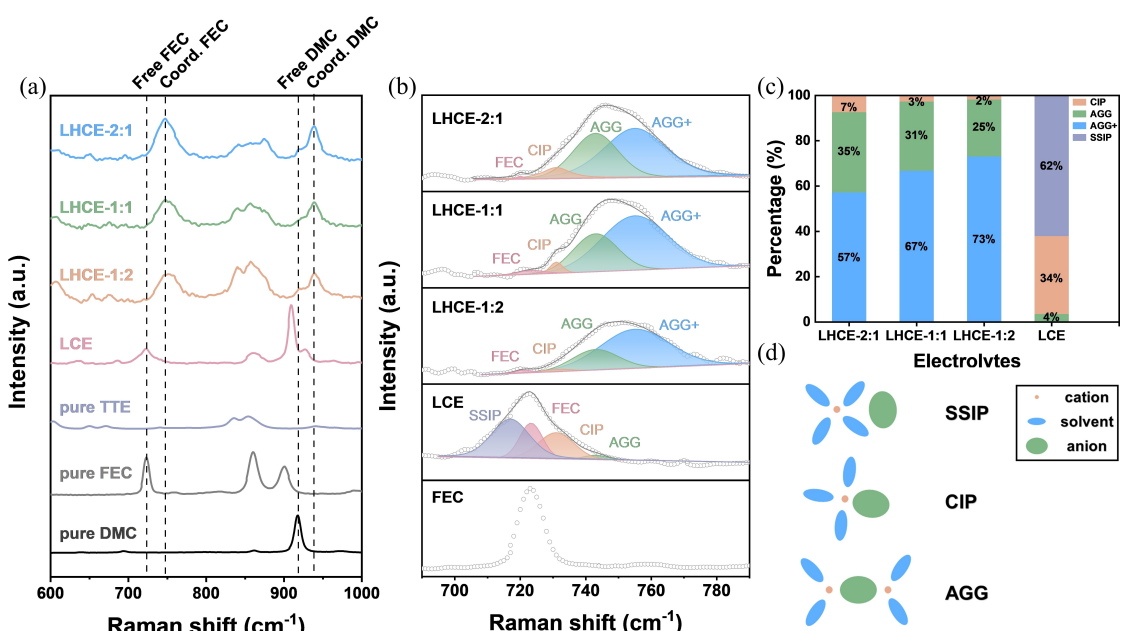


**Figure 2.** (a) Raman spectra of LHCEs and solvents to investigate the coordination; (b) Raman spectra of different electrolytes (LHCE-2:1, LHCE-1:1, LHCE-1:2 and LCE) and the solvent (FEC) to show the proportions of the solvation structures; (c) Proportion of SSIP, CIP, AGG and AGG+; (d) Schematics for three common solvation configurations.

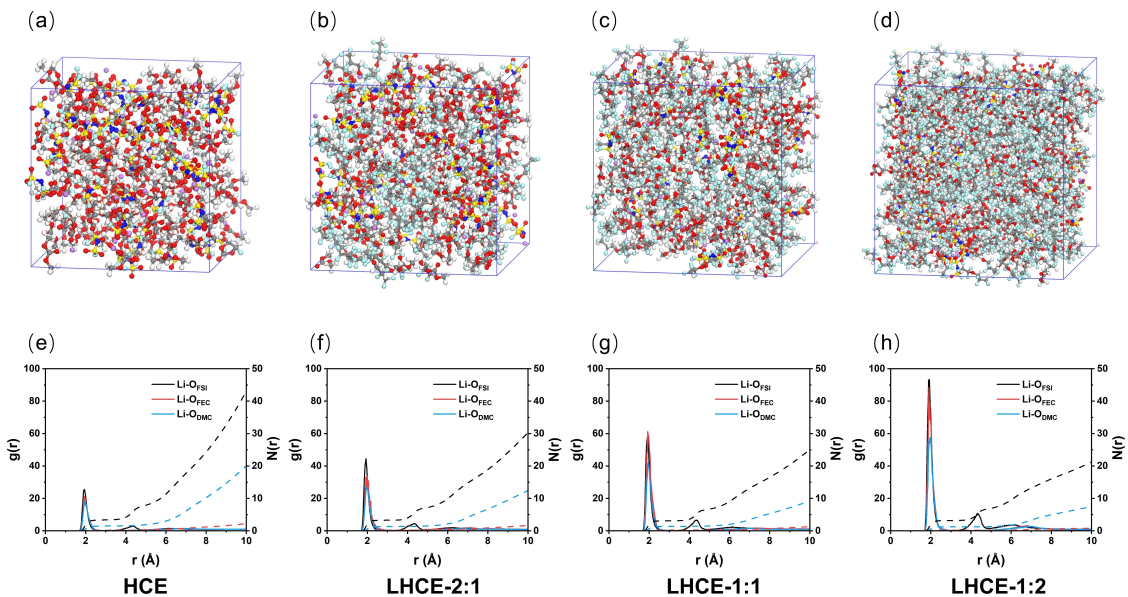


**Figure 3.** (a-d) Snapshots of spatial distribution and (e-h) radial distribution functions of O atoms in DMC-based HCE and LHCEs obtained from MD simulations: (a,e) HCE (without diluent); (b,f) LHCE-2:1; (c,g) LHCE-1:1; (d,h) LHCE-1:2.

LHCE-2:1, the peak of Li–O<sub>FSI</sub> is higher than Li–O<sub>DMC</sub> and Li–O<sub>FEC</sub>, indicating a stronger attraction between FSI<sup>-</sup> with Li<sup>+</sup> compared to DMC/FEC with Li<sup>+</sup>. The peaks of Li–O<sub>DMC</sub> in HCE, LHCE-2:1, LHCE-1:1, and LHCE-1:2 are 1.97, 1.95, 1.95, and 1.99 Å, with coordination numbers of 0.50, 0.37, 0.43, and 0.57, respectively. It can be observed that in LHCE-1:2, the coordination number significantly increases, implying a greater association of Li<sup>+</sup> with DMC. This may be due to the fact that TTE contains a large number of fluorine atoms with a strong electron-withdrawing effect and does not coordinate with Li<sup>+</sup>, and dipole-dipole interactions between diluent and solvents lead to partial splitting of AGGs,<sup>[34]</sup> which results in a larger Li–O<sub>DMC</sub> distance and a higher Li–O<sub>DMC</sub> coordination number. RDF elucidates that excessive addition of diluent significantly affects the coordination of Li<sup>+</sup> with DMC and the number of AGGs, altering the primary solvation structure, thereby forming a solvent/anion-derived SEI.

Figure 4 depicts the Li plating/stripping and CE curves of Li||Cu cells at a current density of 1 mA cm<sup>-2</sup> and areal capacity of 1 mAh cm<sup>-2</sup> under a cutoff potential of 1.0 V for different electrolytes. As shown in Figure 4a, LHCE-2:1 exhibits the best Li plating/stripping stability with an average CE of 98.0% after 100 cycles. Moreover, as illustrated in Figure 4b, LHCE-2:1 shows no significant overpotential increase during cycling. In contrast, LHCE-1:1, LHCE-1:2, and LCE display noticeable Coulombic efficiency decay after 68, 63, and 58 cycles, respectively, with average CEs of 96.1%, 96.6%, and 93.1%. Comparing Figure 4b-d and Figure S1, it is observed that LHCE-1:2 exhibits higher overpotential during cycling, which is unfavorable for uniform lithium deposition. Additionally, LCE shows significant overpotential variation during 50 cycles, indicating unstable SEI formation. Thus, whether from the perspective of overpotential or long-term CE, LHCE-2:1 demonstrates the best cycling stability. The surface morphologies of Li

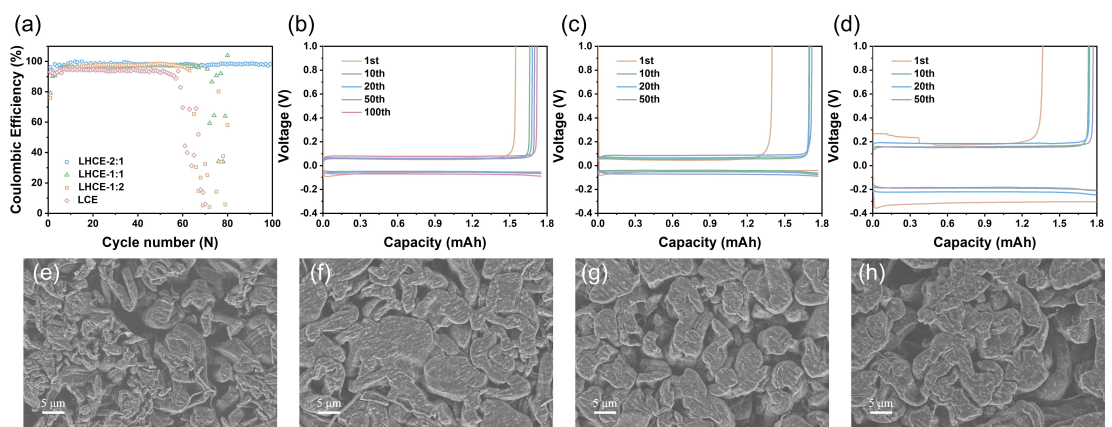


**Figure 4.** (a) Coulombic efficiency of Li||Cu cells in four different electrolytes; (b-d) Voltage profiles for the Li||Cu cells cycled in (b) LHCE-2:1, (c) LHCE-1:1 and (d) LHCE-1:2. (e-h) SEM images of the deposited Li on Cu foil at 0.5 mA cm<sup>-2</sup> and 2.0 mAh cm<sup>-2</sup> in (e) LCE, (f) LHCE-2:1, (g) LHCE-1:1 and (h) LHCE-1:2.

deposition on copper foil are observed via SEM (Figure 4e-h). As shown in Figure 4e, a porous and loose deposition morphology with abundant Li dendrites increases the surface area of lithium metal and electrolyte, potentially leading to more side reactions. In contrast, Li deposit in LHCEs appears denser and more blocky rather than dendritic (Figure 4f-h). We also observe that with the increase in diluent addition, the density of Li deposition decreases. Therefore, the denser nodule-like deposition morphology in LHCE-2:1 is advantageous for reducing side reactions with the electrolyte, thus improving the anodic stability against lithium metal anode.

To verify the stability of the electrolytes with Li metal anode, galvanostatic charge/discharge tests are performed on  $\text{Li}||\text{Li}$  symmetric cells at a current density of  $0.2/0.5 \text{ mA cm}^{-2}$  and an area capacity of  $0.2/0.5 \text{ mAh cm}^{-2}$  (Figure 5a, 5d and S2). At a current density of  $0.2 \text{ mA cm}^{-2}$ , the initial overpotential of LCE is 20 mV (Figure S2), and there is a continuous increase in overpotential after 200 h, indicating the absence of a stable SEI interface on the lithium anode surface. Additionally, at approximately 550 h, the overpotential increases to 100 mV and suddenly drops to 25 mV, indicating that lithium dendrites have penetrated the separator, resulting in internal short-circuiting of the battery. In contrast, all three LHCEs maintain an overpotential of less than 20 mV during the Li plating/stripping lasting up to 1200 h, with only slight polarization increase. Over such an extended testing period, the inevitable reactions between highly reactive lithium and the electrolyte contribute to the slight polarization increase. LHCEs enhance the stability of Li metal anode against DMC-induced instability. This is partly owing to the unique solvation structure within the LHCE systems. Additionally, the presence of FEC in the electrolyte positively contributes to stabilizing the formation of the SEI, further bolstering its stability. Furthermore, at a current density of  $0.5 \text{ mA cm}^{-2}$ , the overpotential of LCE remains stable at around 80 mV within 250 h, followed by voltage fluctuations and short-circuit phenomena. In LHCEs, the initial overpotential of LHCE-1:2 is higher, and the higher polarization voltage indicates a thicker SEI layer. The possible reason is that the

unstable SEI results in continuous side reactions between the lithium anode and the electrolyte to form a new SEI.<sup>[35]</sup> The overpotential of LHCE-2:1 does not significantly increase within 800 h, while LHCE-1:1 and LHCE-1:2 show rapid increases in overpotential at 700 h and 650 h, respectively. The polarization rapidly increases, followed by short-circuiting, indicating that LHCE-2:1 exhibits the best stability with the lithium metal anode.

Figure 6a-b show the long-term cycling curves of the  $\text{Li}||\text{LFP}$  cells at different rates. At 1 C (Figure 6a), the  $\text{Li}||\text{LFP}$  cells using LHCE-2:1, LHCE-1:1, LHCE-1:2 and LCE exhibit the initial discharge capacities of 141, 153.4, 148.4 and  $148.1 \text{ mAh g}^{-1}$ , respectively. After 500 cycles, the capacities decline to 123.4, 120.2, 109.3 and  $87.1 \text{ mAh g}^{-1}$ , corresponding to the capacity retentions of 87.5%, 78.4%, 73.7% and 58.8%, respectively. From the voltage profile of  $\text{Li}||\text{LFP}$  cells cycled in three electrolytes at 1 C (Figure S3), it is clear that the cell with LHCE-2:1 exhibits the highest capacity retentions, indicating that different diluent additions have an effect on capacity retention. Similarly, the  $\text{Li}||\text{LFP}$  cells with LHCEs exhibit the discharge capacities of 124.9, 121.5 and  $121.6 \text{ mAh g}^{-1}$  at 3 C, respectively (Figure 6b). After 1200 charge/discharge cycles, the capacities decline to 87, 84.9 and  $76.3 \text{ mAh g}^{-1}$ , corresponding to the capacity retentions of 69.7%, 69.9% and 62.7%, respectively. It is clear that LHCE-1:2 shows significant capacity decay after 1200 cycles, and the capacity retention is the lowest regardless of rates. As for LCE, it exhibits a rapid Coulombic efficiency decline after approximately 300 cycles. Figure 6c illustrates the rate performance of the the  $\text{Li}||\text{LFP}$  cells, with the first three circles being the formation cycles at 0.1 C. The rate performance of three LHCEs is similar, and all have a specific capacity of about  $125 \text{ mAh g}^{-1}$  at 5 C, which indicates that the different diluent additions have a minimal influence on the rate performance of the cells. However, after cycling at 5 C, LCE is unable to charge or discharge when returned to 0.2 C.

To further explore the compatibility of LHCE with high-voltage cathodes, we assemble  $\text{Li}||\text{NCM622}$  cells using LHCE-2:1. At a mass loading of  $2.0 \text{ mg cm}^{-2}$  for NCM622 and at 0.5 C

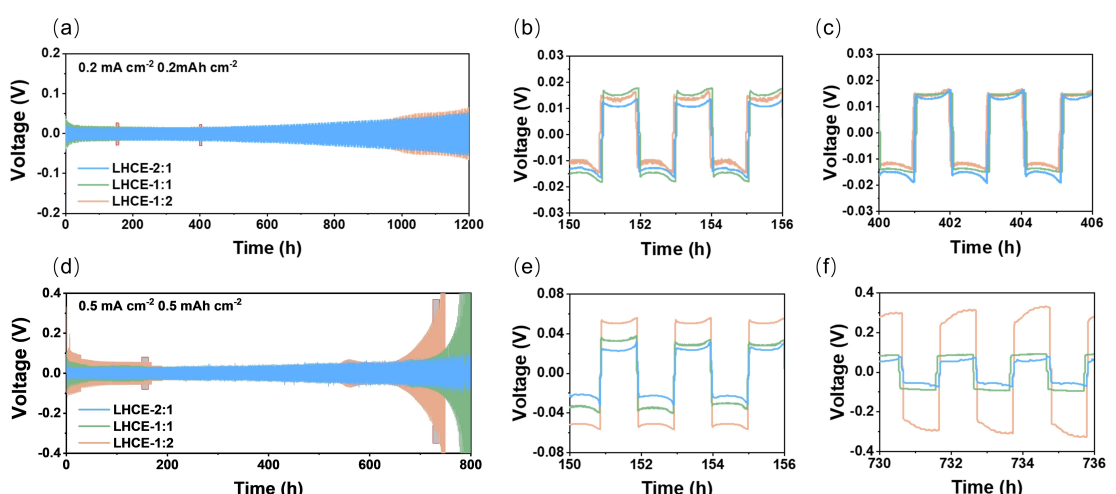
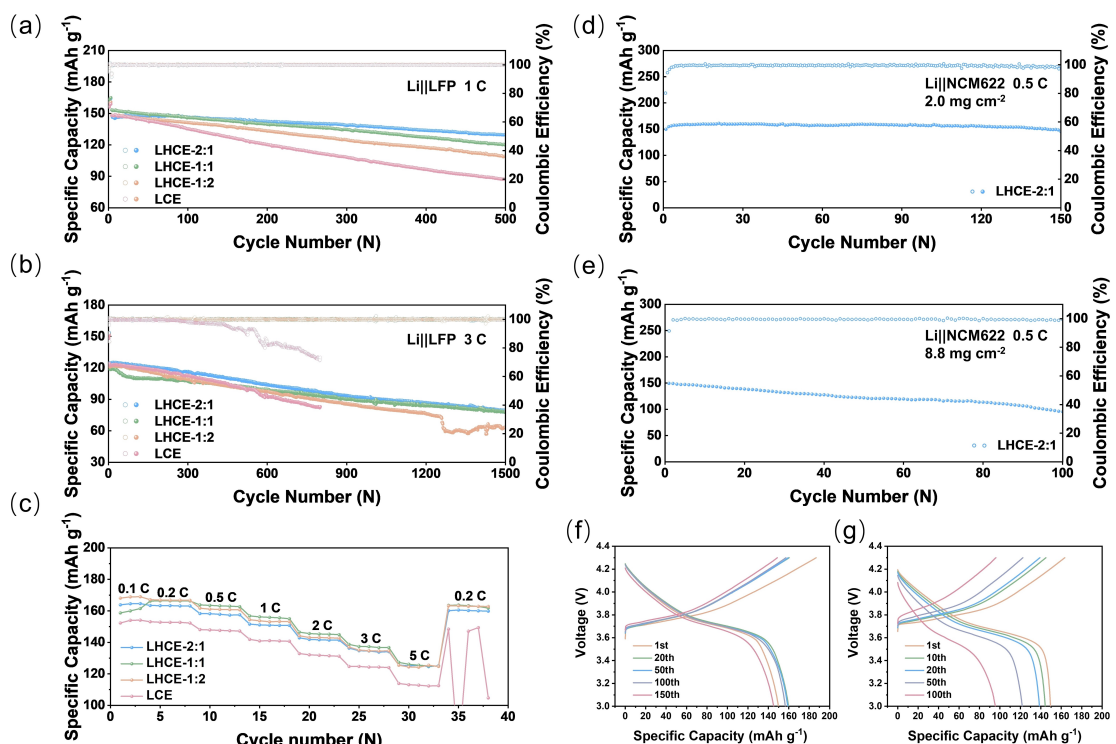


Figure 5. Galvanostatic charge/discharge voltage profiles of  $\text{Li}||\text{Li}$  cells at (a-c):  $0.2 \text{ mA cm}^{-2}, 0.2 \text{ mAh cm}^{-2}$ ; (d-f):  $0.5 \text{ mA cm}^{-2}, 0.5 \text{ mAh cm}^{-2}$ .



**Figure 6.** (a–b) Cycling curves of the Li||LFP cells at 1 C and 3 C; (c) rate capabilities of Li||LFP cells; (d–e) cycling curves of the Li||NCM622 cells at 0.5 C with different mass loadings in LHCE-1:2; (d) 2.0 mg cm⁻² and (e) 8.8 mg cm⁻². (f–g) voltage profiles of Li||NCM622 cells cycled in LHCE-1:2 at 0.5 C except for three formation cycles: (d) LHCE-2:1; (e) LHCE-1:1; (f) LHCE-1:2.

(Figure 6d and 6f), the initial specific capacity of the cell is 149.84 mAh g⁻¹, which subsequently increases to around 160 mAh g⁻¹. After 150 cycles, the specific capacity decreases to 145.17 mAh g⁻¹, resulting in a capacity retention of 96.9%. Afterwards, we use a higher mass loading of 8.8 mg cm⁻² for NCM622 (Figure 6e and 6g). The initial specific capacity of the cell is 149.47 mAh g⁻¹, and after 100 cycles, it decreases to 95.49 mAh g⁻¹, resulting in a capacity retention of 63.9%. The performance of Li||NCM622 cells assembled with the other two electrolytes is shown in Figure S4, and rapid capacity decay occurs in LHCE-1:1 and LHCE-1:2, accompanied by rapid Coulombic decay in LHCE-1:2. LCE is incompatible with NCM622. Additionally, a Li||LFP pouch cell is assembled with LHCE-2:1 (Figure S5), and the pouch cell successfully illuminates LED lights, demonstrating the potential of the electrolyte for industrial applications.

The surface morphologies of the cycled Li anodes after 100 charge/discharge cycles at 1 C for Li||LFP cells are observed using SEM. It is evident that the addition of TTE significantly alters the morphology of the cycled Li anodes (Figure S6). LHCE-2:1, with low TTE content, results in a denser and smoother Li deposition morphology. Conversely, in LHCE-1:2, where the TTE content is too high, pronounced Li dendrite growth becomes apparent. This phenomenon can be ascribed to the relatively lower ionic conductivity of LHCE-1:2, where the thicker TTE secondary sheath tends to induce uneven potential distribution during charge and discharge processes, leading to irregular lithium deposition on the surface and

lithium dendrite growth. Lithium dendrite, due to its larger surface area, is more prone to react with the electrolyte, irreversibly consuming active materials and reducing the Coulombic efficiency and cycling stability of the battery.

XPS is utilized to analyze the chemical composition of the SEI formed on the lithium metal surface for the Li||LFP cells in three different electrolytes after 100 charge/discharge cycles. The proportions of C, F, and O are shown in Figure S7a, and LHCE-2:1 has the highest F content and the lowest O content. Figure 7a shows the C 1s spectra, and C–C, C–O, C=O and ROCO<sub>2</sub>Li bonds mainly originate from the decomposition of DMC. The most significant distinction among different TTE addition amounts is the varying content of ROCO<sub>2</sub>Li, and the mechanical strength of ROCO<sub>2</sub>Li is insufficient to alleviate SEI fractures, hence based on the content of ROCO<sub>2</sub>Li in the C 1s spectra, LHCE-2:1 exhibits better anodic stability for lithium.<sup>[36]</sup> F 1s spectra in Figure 7b indicate the presence of fluorinated organic compounds and a high proportion of LiF in the SEI, which can explain the better stability of all three LHCEs against lithium. This is because LiF serves as a proficient insulator,<sup>[37–38]</sup> effectively impeding electron leakage across the interface, which is widely recognized that electron leakage is one of the critical factors contributing to sustained electrolyte decomposition and Li dendrite formation in lithium batteries.<sup>[39]</sup> Besides, LiF demonstrates higher mechanical strength, effectively inhibiting Li dendrite growth.<sup>[40]</sup> Therefore, LiF-rich SEI reduces continuous electrolyte decomposition and ensures long-term stability against the lithium metal anode. LiF primarily originates

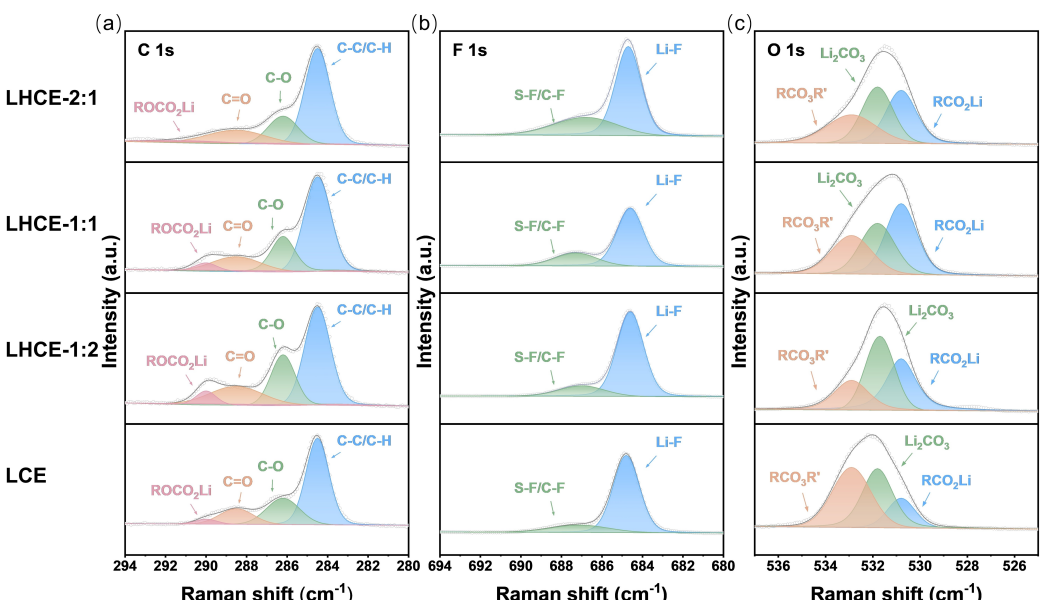


Figure 7. XPS spectra of C 1s (a), F 1s (b) and O 1s (c) of the cycled Li anode in different electrolytes after 100 cycles at 1 C for Li||LFP cells.

from the introduction of TTE, which weakens the interaction between  $\text{Li}^+$ -solvent, thus  $\text{FSI}^-$  appears in the primary solvation sheath, while TTE does not interact with  $\text{Li}^+$  and exists in the secondary solvation sheath. Additionally, the dipole-dipole interaction between TTE and solvent causes the solvent to exhibit a tendency to be pulled away from the primary solvation sheath by TTE, thereby forming an anion-derived  $\text{LiF}$ -rich SEI layer, rather than the SEI generated from solvent decomposition.<sup>[41]</sup> The O 1s spectra in Figure 7c reveal a combination of organic and inorganic components in the SEI layer. Strangely, although the LHCE-1:2 has the highest content of  $\text{Li}_2\text{CO}_3$ , it exhibits the poorest cycling stability in the batteries. One possible reason is that for the SEI of LHCE-1:2, the proportion of  $\text{Li}_2\text{CO}_3$  in the inorganic phase is higher than  $\text{LiF}$ , however, the energy barrier for  $\text{Li}^+$  diffusion on the surface of  $\text{LiF}$  is 0.09 eV lower than that of  $\text{Li}_2\text{CO}_3$ , which facilitates lithium transport.<sup>[42]</sup> Moreover, the surface energy of  $\text{LiF}$  is three times higher than that of  $\text{Li}_2\text{CO}_3$ , suggesting that the lithium metal surface containing  $\text{LiF}$  promotes to form a uniform SEI. According to XPS, the ratio of F:C for LHCE-2:1, LHCE-1:1 and LHCE-1:2 is 1.25, 1.22 and 0.96, respectively. In the LHCE with a high TTE addition (LHCE-1:2), the F content is decreased, possibly due to the excessive TTE, which affects the formation of the anion-derived SEI. The possible reason is that RDF shows a higher coordination number of  $\text{Li}-\text{O}_{\text{DMC}}$  in LHCE-1:2 (Figure 3), leading to an increase in the component of SEI from solvent decomposition and a decrease in the  $\text{LiF}$  component of SEI from anion decomposition. This corresponds to its relatively low F:C ratio. Consequently, the excessive TTE influences the anodic stability against lithium and cycling performance of the cells by impacting the performance of the SEI. From the O 1s spectra, it can also observe that LCE has a high proportion of  $\text{RCO}_3\text{R}'$ , indicating that the SEI formed in LCE contains more O-containing organic compounds. Additionally, from the elemen-

tal ratio, the proportion of O in LCE is also higher. This explains why LCE also has a higher proportion of  $\text{LiF}$ , but still exhibits poor cycling performance against lithium.

The chemical compositions and elemental proportions of the CEI layer on the surface of the cycled LFP cathode in three different electrolytes are analyzed by XPS after 100 charge/discharge cycles at 1 C. The CEI formed in LCE exhibits the lowest proportion of F and the highest proportion of C. For C 1s spectra (Figure S7b and 8a), the appearance of  $\text{CF}_3$  at 290.8 eV can be attributed to the decomposition of PVDF and FEC.<sup>[43]</sup> The low intensity of the C–F bond indicates effective suppression of the decomposition of PVDF and FEC in LHCEs, which also provides an explanation for the better stability against lithium metal anode of the three electrolytes. In LCE, a higher proportion of C–F intensity is evident, suggesting the participation of FEC in the construction of the CEI. Observing the F 1s spectra (Figure 8b), three LHCEs exhibit a relatively high intensity of S–F bond, which may arise from the decomposition of  $\text{LiFSI}$ , indicating that the formation of the CEI within LHCEs is also anion-derived.<sup>[44]</sup> The surface of the cycled LFP cathode in LHCE-1:2 contains more S–F/C–F bonds, suggesting that more TTE may have participated in the construction of the CEI.<sup>[45]</sup> It has been reported that an F-rich CEI will stabilize the cathode at high voltage.<sup>[46]</sup> According to XPS, the ratio of F:C for LHCE-2:1, LHCE-1:1 and LHCE-1:2 is 0.47, 0.45 and 0.53, respectively. Additionally, the content of F in the CEI is significantly lower than that in the SEI. It has been reported that the presence of a large amount of high-resistance  $\text{LiF}$  on the cathode surface is detrimental to  $\text{Li}^+$  transport, leading to capacity decay.<sup>[47]</sup> Furthermore, the similar contents of C, F, and O in the CEI of all three LHCEs imply that the different amounts of diluent have a relatively minor impact on the CEI.

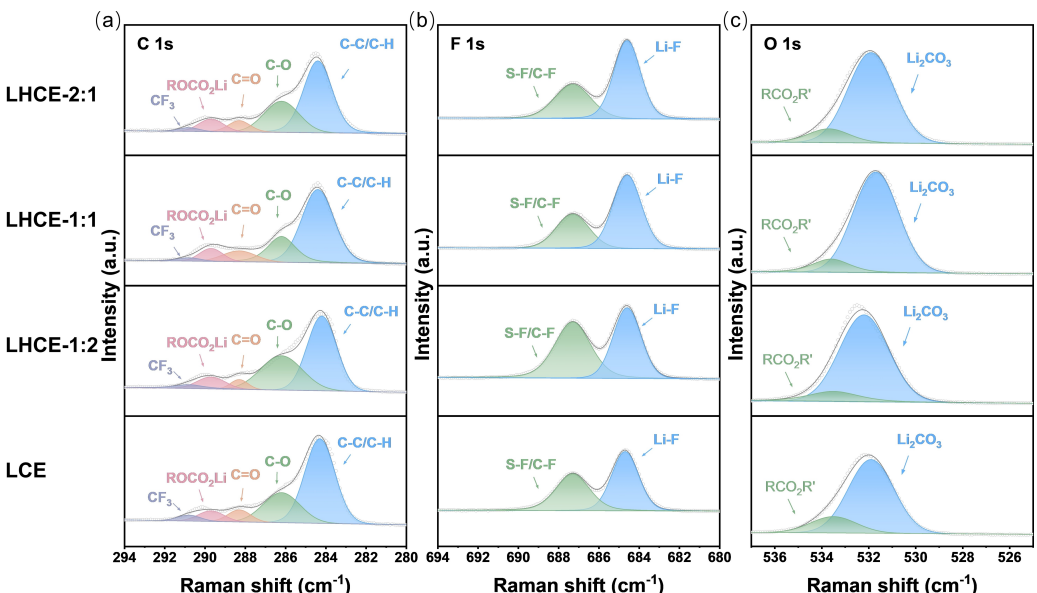


Figure 8. XPS spectra of C 1s (a), F 1s (b) and O 1s (c) of the cycled LFP cathode in different electrolytes after 100 cycles at 1 C for Li || LFP cells.

## Conclusions

In this work, DMC-based LHCEs with different diluent addition ratios are systematically investigated and compared. Compared to LCE, LHCEs exhibit a higher proportion of ClPs and AGGs in the solvation structure, along with a higher  $\text{Li}^+$  transference number. This indicates that the introduction of TTE weakens the interaction of  $\text{Li}^+$ -solvent while enhancing the interaction of  $\text{Li}^+$ -FSI<sup>-</sup>, thereby promoting the formation of anion-derived SEI and improving the stability of DMC-based electrolytes against lithium. Different diluent addition ratios predominantly influence the battery performance by modulating the characteristics of the SEI. An excess of TTE enhances the interaction between  $\text{Li}^+$  and DMC while reducing the fluorine content in the SEI, which hinders the formation of anion-derived SEI and adversely affects the stability against the lithium anode and the cycling performance of the battery. Therefore, the diluent addition ratio in the LHCE system is also a factor that should be considered. LHCE-2:1 improves the Coulombic efficiency and the cycling stability in lithium metal batteries. Furthermore, it exhibits excellent capacity retention in Li || NCM622 cells at 0.5 C after 150 cycles.

## Acknowledgements

This work was supported by the Development Program of Zhejiang Province (No. 2022C01071) and the National Natural Science Foundation of China (Grant No. 51971201, 52073253, U20A20126, 52103350).

## Conflict of Interests

The authors declare no conflict of interest.

## Data Availability Statement

The data that support the findings of this study are available from the corresponding author upon reasonable request.

**Keywords:** Localized high concentration electrolytes · solid electrolyte interphase · lithium metal batteries

- [1] W. Xu, J. L. Wang, F. Ding, X. L. Chen, E. Nasybutin, Y. H. Zhang, J. G. Zhang, *Energy Environ. Sci.* **2014**, *7*, 513–537.
- [2] R. Zhang, N. W. Li, X. B. Cheng, Y. X. Yin, Q. Zhang, Y. G. Guo, *Adv. Sci.* **2017**, *4*, 1600445.
- [3] L. M. Suo, Y. S. Hu, H. Li, M. Armand, L. Q. Chen, *Nat. Commun.* **2013**, *4*, 1481.
- [4] S. R. Chen, J. M. Zheng, D. H. Mei, K. S. Han, M. H. Engelhard, W. G. Zhao, W. Xu, J. Liu, J. G. Zhang, *Adv. Mater.* **2018**, *30*, 1706102.
- [5] X. L. Fan, L. Chen, X. Ji, T. Deng, S. Hou, J. Chen, J. Zheng, F. Wang, J. J. Jiang, K. Xu, C. S. Wang, *Chem* **2018**, *4*, 174–185.
- [6] T. Li, X. Q. Zhang, P. Shi, Q. Zhang, *Joule* **2019**, *3*, 2647–2661.
- [7] H. Wu, H. Jia, C. Wang, J. Zhang, W. Xu, *Adv. Energy Mater.* **2021**, *11*, 2003092.
- [8] S. Ko, Y. Yamada, A. Yamada, *Joule* **2021**, *5*, 998–1009.
- [9] Z. Chang, Y. Qiao, H. Deng, H. J. Yang, P. He, H. S. Zhou, *Joule* **2020**, *4*, 1776–1789.
- [10] J. H. Wang, Y. Yamada, K. Sodeyama, E. Watanabe, K. Takada, Y. Tateyama, A. Yamada, *Nat. Energy* **2018**, *3*, 22–29.
- [11] C. Zhang, S. C. Gu, D. F. Zhang, J. B. Ma, H. Zheng, M. Y. Zheng, R. T. Lv, K. Yu, J. Q. Wu, X. M. Wang, Q. H. Yang, F. Y. Kang, W. Lv, *Energy Storage Mater.* **2022**, *52*, 355–364.
- [12] M. X. He, X. Li, X. F. Yang, C. H. Wang, M. L. Zheng, R. Y. Li, P. J. Zuo, G. P. Yin, X. L. Sun, *Adv. Energy Mater.* **2021**, *11*, 2101004.
- [13] Y. L. Jie, X. D. Ren, R. G. Cao, W. B. Cai, S. H. Jiao, *Adv. Funct. Mater.* **2020**, *30*, 1910777.
- [14] Y. Liu, Y. T. Huang, X. Xu, Y. Liu, J. H. Yang, J. W. Lai, J. K. Shi, S. X. Wang, W. Z. Fan, Y. P. Cai, Y. Q. Lan, Q. F. Zheng, *Adv. Funct. Mater.* **2023**, *33*, 2303667.
- [15] J. Moon, D. O. Kim, L. Bekaert, M. Song, J. Chung, D. Lee, A. Hubin, J. Lim, *Nat. Commun.* **2022**, *13*, 4538.
- [16] M. M. Fang, B. Y. Du, X. R. Zhang, X. B. Dong, X. Y. Yue, Z. Liang, *Angew. Chem. Int. Ed.* **2024**, *63*, e202316839.
- [17] X. J. Chen, L. Qin, J. N. Sun, S. W. Zhang, D. Xiao, Y. Y. Wu, *Angew. Chem. Int. Ed.* **2022**, *61*, e202207018.

- [18] K. Dokko, N. Tachikawa, K. Yamauchi, M. Tsuchiya, A. Yamazaki, E. Takashima, J.-W. Park, K. Ueno, S. Seki, N. Serizawa, M. Watanabe, *J. Electrochem. Soc.* **2013**, *160*, A1304.
- [19] X. D. Ren, S. R. Chen, H. Lee, D. H. Mei, M. H. Engelhard, S. D. Burton, W. G. Zhao, J. M. Zheng, Q. Li, M. S. Ding, M. Schroeder, J. Alvarado, K. Xu, Y. S. Meng, J. Liu, J. G. Zhang, W. Xu, *Chem* **2018**, *4*, 1877–1892.
- [20] Z. H. Piao, R. H. Gao, Y. Q. Liu, G. M. Zhou, H. M. Cheng, *Adv. Mater.* **2023**, *35*, 2206009.
- [21] S. C. Zhang, S. Y. Li, Y. Y. Lu, *eScience* **2021**, *1*, 163–177.
- [22] Y. K. Wang, Z. M. Li, Y. P. Hou, Z. M. Hao, Q. Zhang, Y. X. Ni, Y. Lu, Z. H. Yan, K. Zhang, Q. Zhao, F. J. Li, J. Chen, *Chem. Soc. Rev.* **2023**, *52*, 2713–2763.
- [23] G. Song, Z. L. Yi, F. Y. Su, L. J. Xie, Z. B. Wang, X. X. Wei, G. N. Xu, C. M. Chen, *ACS Energy Lett.* **2023**, *8*, 1336–1343.
- [24] J. B. Hou, M. Yang, D. Y. Wang, J. L. Zhang, *Adv. Energy Mater.* **2020**, *10*, 1904152.
- [25] Z. Yuan, A. Chen, J. Liao, L. Song, X. Zhou, *Nano Energy* **2024**, *119*, 109088.
- [26] H. K. Bergstrom, B. D. McCloskey, *ACS Energy Lett.* **2024**, *9*, 373–380.
- [27] N. N. Sun, R. H. Li, Y. Zhao, H. K. Zhang, J. H. Chen, J. T. Xu, Z. D. Li, X. L. Fan, X. Y. Yao, Z. Peng, *Adv. Energy Mater.* **2022**, *12*, 2200621.
- [28] K. M. Diederichsen, E. J. McShane, B. D. McCloskey, *ACS Energy Lett.* **2017**, *2*, 2563–2575.
- [29] Y. F. Zhai, W. S. Hou, M. M. Tao, Z. T. Wang, Z. Y. Chen, Z. Zeng, X. Liang, P. Paoprasert, Y. Yang, N. Hu, S. F. Song, *Adv. Mater.* **2022**, *34*, 2205560.
- [30] H. Zhang, C. M. Li, M. Pisycz, E. Coya, T. Rojo, L. M. Rodriguez-Martinez, M. Armand, Z. B. Zhou, *Chem. Soc. Rev.* **2017**, *46*, 797–815.
- [31] L. F. Zou, P. Y. Gao, H. P. Jia, X. Cao, H. P. Wu, H. Wang, W. G. Zhao, B. E. Matthews, Z. J. Xu, X. L. Li, J. G. Zhang, W. Xu, C. M. Wang, *ACS Appl. Mater. Interfaces* **2022**, *14*, 4111–4118.
- [32] Z. C. Wu, R. H. Li, S. Q. Zhang, L. Lv, T. Deng, H. Zhang, R. X. Zhang, J. J. Liu, S. H. Ding, L. W. Fan, L. X. Chen, X. L. Fan, *Chem* **2023**, *9*, 650–664.
- [33] C. M. Efaw, Q. Wu, N. Gao, Y. G. Zhang, H. Y. Zhu, K. Gering, M. F. Hurley, H. Xiong, E. Y. Hu, X. Cao, W. Xu, J. G. Zhang, E. J. Dufek, J. Xiao, X. Q. Yang, J. Liu, Y. Qi, B. Li, *Nat. Mater.* **2023**, *22*, 1531–1539.
- [34] F. H. Ren, Z. D. Li, J. H. Chen, P. Huguet, Z. Peng, S. Deabate, *ACS Appl. Mater. Interfaces* **2022**, *14*, 4211–4219.
- [35] Y. Jin, P. M. L. Le, P. Gao, Y. Xu, B. Xiao, M. H. Engelhard, X. Cao, T. D. Vo, J. Hu, L. Zhong, B. E. Matthews, R. Yi, C. Wang, X. Li, J. Liu, J.-G. Zhang, *Nat. Energy* **2022**, *7*, 718–725.
- [36] Q. K. Zhang, X. Q. Zhang, J. Wan, N. Yao, T. L. Song, J. Xie, L. P. Hou, M. Y. Zhou, X. Chen, B. Q. Li, R. Wen, H. J. Peng, Q. Zhang, J. Q. Huang, *Nat. Energy* **2023**, *8*, 725–735.
- [37] Z. H. Wu, C. Y. Wang, Z. Y. Hui, H. D. Liu, S. Wang, S. C. Yu, X. Xing, J. Holoubek, Q. S. Miao, H. L. Xin, P. Liu, *Nat. Energy* **2023**, *8*, 340–350.
- [38] J. Tan, J. Matz, P. Dong, J. F. Shen, M. X. Ye, *Adv. Energy Mater.* **2021**, *11*, 2100046.
- [39] K. Leung, *J. Phys. Chem. C* **2013**, *117*, 1539–1547.
- [40] Y. L. Xiao, B. Han, Y. Zeng, S. S. Chi, X. Z. Zeng, Z. J. Zheng, K. Xu, Y. H. Deng, *Adv. Energy Mater.* **2020**, *10*, 1903937.
- [41] Q. J. Sun, Z. Cao, Z. Ma, J. L. Zhang, H. R. Cheng, X. R. Guo, G. Park, Q. Li, E. Q. Xie, L. Cavallo, Y. Sun, J. Ming, *ACS Energy Lett.* **2022**, *7*, 3545–3556.
- [42] S. Choudhury, L. A. Archer, *Adv. Electron. Mater.* **2016**, *2*, 1500246.
- [43] M. Liu, X. Li, B. Zhai, Z. Zeng, W. Hu, S. Lei, H. Zhang, S. Cheng, J. Xie, *Batteries & Supercaps* **2022**, *5*, e202100407.
- [44] M. Fang, B. Du, X. Zhang, X. Dong, X. Yue, Z. Liang, *Angew. Chem. Int. Ed.* **2024**, *63*, e202316839.
- [45] S. D. Zhu, J. Chen, *Energy Storage Mater.* **2022**, *44*, 48–56.
- [46] W. R. Zhang, V. Koverga, S. F. Liu, J. G. Zhou, J. Wang, P. X. Bai, S. Tan, N. K. Dandu, Z. Y. Wang, F. Chen, J. L. Xia, H. L. Wan, X. Y. Zhang, H. C. Yang, B. L. Lucht, A. Li, X. Q. Yang, E. Y. Hu, S. R. Raghavan, A. T. Ngo, C. S. Wang, *Nat. Energy* **2024**, DOI: 10.1038/s41560-41023-01443-41560.
- [47] W. G. Zhao, J. M. Zheng, L. F. Zou, H. P. Jia, B. Liu, H. Wang, M. H. Engelhard, C. M. Wang, W. Xu, Y. Yang, J. G. Zhang, *Adv. Energy Mater.* **2018**, *8*, 1800297.

Manuscript received: April 8, 2024

Accepted manuscript online: April 22, 2024

Version of record online: May 23, 2024